Nanoscale Advances

ROYAL SOCIETY OF CHEMISTRY

PAPER

View Article Online
View Journal | View Issue

Cite this: *Nanoscale Adv.*, 2025, **7**, 2742

Battery-type $CuCo_2O_4$/CoS nanograss arrays as a binder-free advanced electrode material for high-performance supercapacitors†

Chandu V. V. Muralee Gopi, ‡[a] Araveeti Eswar Reddy, ‡[b] Sunkara Srinivasa Rao, [c] K. V. G. Raghavendra,[d] Maduru Suneetha,*[e] Hee-Je Kim*[d] and R. Ramesh *[f]

This study uses a facile one-step hydrothermal method to successfully synthesize hierarchical dandelion flower-like $CuCo_2O_4$/CoS structures on Ni foam. The composite exhibits a unique dandelion flower-like architecture comprising interconnected nanograss arrays (NGAs), resulting in a significantly higher surface area than individual $CuCo_2O_4$ and CoS electrodes. Electrochemical characterization reveals that the $CuCo_2O_4$/CoS electrode exhibits superior electrochemical performance, demonstrating battery-type behavior with well-defined redox peaks in cyclic voltammetry and distinct plateaus in galvanostatic charge–discharge curves. The composite electrode delivers a high specific capacity of 217.86 mA h g^{-1} at a current density of 6 mA cm^{-2}, surpassing the performance of individual $CuCo_2O_4$ (142.54 mA h g^{-1}) and CoS (160.37 mA h g^{-1}) electrodes. Moreover, the composite electrodes exhibit outstanding cycling life, retaining 86.23% of their initial capacity in over 3000 cycles. Electrochemical impedance spectroscopy analysis confirms lower charge transfer resistance and solution resistance for the composite electrode, indicating improved charge transfer kinetics and ion diffusion. These findings demonstrate that the hierarchical $CuCo_2O_4$/CoS composite holds significant promise as a high-performance battery-type electrode material for supercapacitor applications.

Received 18th January 2025
Accepted 16th March 2025

DOI: 10.1039/d5na00070j

rsc.li/nanoscale-advances

1 Introduction

The growing emphasis on environmental protection and the need for sustainable energy solutions have urged significant research and development in technologies related to energy generation, storage, and conservation.[1,2] Electrochemical capacitors, often called supercapacitors, are emerging as a leading contender for advanced energy storage solutions due to their numerous benefits. These include their eco-friendly nature, exceptional power delivery capabilities, rapid charging and discharging times, high current handling capacity, and extended lifespan compared to traditional batteries.[3–6] Supercapacitors are broadly classified into two types: electrochemical double-layer capacitors (EDLCs), utilizing carbon-based materials,[7,8] and pseudocapacitors (PCs), employing conductive polymers or transition metal compounds.[9–12] EDLCs rely on ion adsorption for energy storage, offering long cycle life and high power density but limited energy density. In contrast, PCs utilize reversible faradaic reactions for charge storage, resulting in significantly higher specific capacitance and energy density than EDLCs.[13]

Furthermore, it has been observed that mixed transition metal oxides often exhibit enhanced properties compared to their single-component or single-phase counterparts, likely due to the synergistic interactions between the multiple metal species, such as $MnCo_2O_4$,[14] $MgCo_2O_4$,[15] $FeCo_2O_4$,[16] $CuCo_2O_4$,[17] $NiCo_2O_4$ (ref. 18) and $ZnCo_2O_4$.[19] Among them, $CuCo_2O_4$ has attracted increased interest due to its natural abundance, low cost, environmental compatibility, and high theoretical capacity.[20] Compared to its individual copper and cobalt oxide counterparts, $CuCo_2O_4$ exhibits enhanced electrochemical activity and electrical conductivity due to multiple oxidation states for both copper and cobalt within its structure.[21,22] Despite these advantages, its theoretical capacitance of 984 F g^{-1} limits its suitability for high-performance supercapacitor

[a]*Department of Electrical Engineering, University of Sharjah, P.O. Box 27272, Sharjah, United Arab Emirates*

[b]*Department of Chemistry, Malla Reddy College of Engineering and Technology, Maisammaguda, Secunderabad, India-500100*

[c]*Department of Electronics and Communication Engineering, Koneru Lakshmaiah Education Foundation, Bowrampet, Hyderabad, Telangana, 500 043, India*

[d]*Department of Electrical Engineering, Pusan National University, Busan, Republic of South Korea. E-mail: heeje@pusan.ac.kr*

[e]*School of Chemical Engineering, Yeungnam University, 280 Daehak-Ro, Gyeongsan, Gyeongbuk, 38541, Republic of Korea. E-mail: msunithachem@gmail.com*

[f]*Department of Chemical Engineering, School of Mechanical, Chemical and Materials Engineering, Adama Science and Technology University, P.O. Box 1888, Adama, Ethiopia. E-mail: ramesh.redrouthu@astu.edu.et*

† Electronic supplementary information (ESI) available. See DOI: https://doi.org/10.1039/d5na00070j

‡ These authors have made an equal contribution to this work.

applications.[22] To improve the capacitance of $CuCo_2O_4$, researchers have investigated various nanostructures, aiming to facilitate rapid ion transport and increase the available surface area for charge storage. For example, $CuCo_2O_4$ nanoparticles demonstrated a high capacitance of 338 F g^{-1} at a current density of 1 A g^{-1} in a study by Pendashteh *et al.*[23] In another investigation, hierarchical nanostructures based on $CuCo_2O_4$ nanobelt morphology exhibited a specific capacitance of 809 F g^{-1}.[17] Despite limitations arising from low conductivity, advancements in core–shell heterostructures have demonstrated improved electrochemical performance in applications. Hierarchical $CuCo_2O_4/MnCo_2O_4$ bilayer spinel heterostructures were fabricated on graphite paper using a two-step hydrothermal process, exhibiting a remarkable specific capacitance of 1434 F g^{-} [et1] at a current density of 0.5 A g^{-1}.[24] A hierarchical $NiCo_2O_4$@MnO_2 composite, synthesized through a multi-step process involving electrospinning, calcination, and hydrothermal treatment, demonstrated high specific capacitance (706.7 F g^{-1} at 3 A g^{-1}) and excellent cycling stability, as reported by Li *et al.*[25] Therefore, controllable synthesis and integrated core/shell heterostructures with superior electrochemical properties are crucial for high-performance electrochemical capacitors. On the other hand, cobalt sulfides (CoSs) like CoS, CoS_2, and Co_3S_4 offer advantages such as high theoretical capacitance (~2356.2 F g^{-1}), low toxicity, and cost-effectiveness.[26] Therefore, combining $CuCo_2O_4$ with hierarchically structured CoS is a promising strategy for advanced battery-type electrodes, leveraging their individual strengths for improved performance and stability.

Herein, we report for the first time a simple one-step hydrothermal method to directly fabricate hierarchical dandelion flower-like $CuCo_2O_4$/CoS structures on Ni foam. The composite material exhibited a higher specific surface area than the bare $CuCo_2O_4$ and CoS materials. The synthesized hierarchical dandelion flower-like $CuCo_2O_4$/CoS composite electrode showed an enhanced electrochemical performance, such as a high specific capacity of 217.86 mA h g^{-1} at 6 mA cm^{-2} and excellent long-term cycle stability (86.23% capacitance retention after 3000 cycles) than $CuCo_2O_4$ and CoS electrodes. The hierarchical $CuCo_2O_4$/CoS dandelion flower-like composite, fabricated through a one-step hydrothermal process, exhibits superior electrochemical properties, showing significant potential for future electronic applications.

2 Experimental

2.1 Materials

Analytical-grade copper(II) nitrate trihydrate ($Cu(No_3)_2 \cdot 3H_2O$), cobalt(II) nitrate hexahydrate ($Co(No_3)_2 \cdot 6H_2O$), (C_2H_5NS), urea (CH_4N_2O), ammonium fluoride (NH_4F), potassium hydroxide (KOH), and Ni foam, all obtained from Sigma-Aldrich, were used without further purification in the experiment.

2.2 Synthesis of $CuCo_2O_4$, CoS and $CuCo_2O_4$/CoS electrodes

Prior to deposition, Ni foams underwent surface cleaning by sonication in 2 M HCl for 30 minutes to eliminate the oxide layer, followed by sequential 10 minute washes in acetone, ethanol, and deionized (DI) water. After that, the cleaned Ni foams were dried in an electric oven overnight. A solution was prepared by combining 0.028 M $Cu(NO_3)_2 \cdot 3H_2O$, 0.1 M $Co(NO_3)_2 \cdot 6H_2O$, 0.4 M C_2H_5NS, 0.4 M CH_4N_2O, and 0.168 M NH_4F in 80 mL of DI water, followed by 30 minutes of stirring to ensure complete dissolution of all components. After transferring the completely dissolved reaction mixture and a thoroughly cleaned Ni foam piece to a Teflon-lined stainless-steel autoclave, the system was maintained at 90 °C for 15 hours. Following deposition, the autoclave was allowed to cool naturally to ambient temperature, after which the Ni foam substrates bearing the deposited active material were retrieved and subjected to repeated ethanol and DI water rinses. Finally, the resulting $CuCo_2O_4$/CoS composite electrodes were annealed at 150 °C for 3 hours in air, with a heating rate of 3 °C min^{-1}. Similarly, bare $CuCo_2O_4$ and CoS were synthesized on Ni foam substrates using analogous procedures and corresponding precursors. The active materials $CuCo_2O_4$, CoS, and $CuCo_2O_4$/CoS, deposited on a Ni foam substrate, exhibited mass loadings of 2.77, 2.7, and 2.8 mg cm^{-2}, respectively.

2.3 Materials characterization

Comprehensive characterization of the materials was carried out using a suite of techniques. Crystalline phases and structural properties were elucidated *via* X-ray diffraction (XRD) analysis using a Bruker D8 Advance system. Morphological features were examined using scanning electron microscopy (SEM) coupled with energy-dispersive X-ray spectroscopy (EDX) for elemental mapping on a Hitachi S-2400 instrument. Transmission electron microscopy (TEM) on a CJ111 instrument provided detailed insights into the microstructure, including lattice fringes and interfacial characteristics. Surface chemical composition was investigated using X-ray photoelectron spectroscopy (XPS) on a VG Scientific ESCALAB 250 system. Finally, Brunauer–Emmett–Teller (BET) surface area and Barrett–Joyner–Halenda (BJH) pore size distribution measurements were performed on a BEL-sorp-Max instrument (BEL, Japan) to assess the materials' textural properties.

2.4 Electrochemical measurements

Electrochemical characterization of the fabricated electrodes was performed using a Biologic-SP150 electrochemical workstation in a three-electrode cell configuration with a 3 M KOH electrolyte. Cyclic voltammetry (CV) was conducted between −0.3 and 0.5 V *vs.* Ag/AgCl at scan rates ranging from 5 to 50 mV s^{-1}. Galvanostatic charge–discharge (GCD) measurements were performed within a potential window of 0 to 0.4 V *vs.* Ag/AgCl, and electrochemical impedance spectroscopy (EIS) was carried out over a frequency range of 0.1 Hz to 500 kHz to investigate the electrochemical behavior of the electrodes further. Specific capacity (Q_{SC}, mA h g^{-1}) for all electrodes was determined using eqn (1).

$$Q_{SC} = \frac{I \times \Delta t}{m \times 3.6} \quad (1)$$

where I (A) is the constant discharge current, Δt (s) signifies the discharge time, and m (g) is the active material mass.[27]

3 Results and discussion

A $CuCo_2O_4$/CoS composite electrode with a unique dandelion flower-like morphology was effectively deposited on a Ni foam substrate through a straightforward one-step hydrothermal process (Scheme 1). This dandelion flower-like structure comprises densely packed nanograss arrays (NGAs). The hierarchical architecture of this composite significantly enhances its electrochemical properties. The high surface area provided by the numerous NGAs maximizes contact with the electrolyte, leading to abundant electroactive sites. Furthermore, the shortened diffusion pathways within the nanograss structure facilitate rapid ion transport within the electrode, resulting in enhanced energy storage performance.

The surface morphologies of $CuCo_2O_4$, CoS, and $CuCo_2O_4$/CoS architectures were investigated using SEM, as presented in Fig. 1. Fig. 1a–f reveal that $CuCo_2O_4$ and CoS active materials deposited on Ni foam exhibit irregular and non-uniform morphologies characterized by nanoparticle-like structures. Both electrode materials display a tendency towards the formation of agglomerated particles, resulting in a surface with numerous voids and micro-gaps. This non-homogeneous distribution of nanoparticles and the presence of significant gaps between them on the Ni foam substrate are not conducive to optimal electrochemical performance. Unlike bare $CuCo_2O_4$ and CoS electrodes, the $CuCo_2O_4$/CoS composite electrode exhibited a unique surface morphology characterized by consistent and uniform coverage over the entire Ni foam substrate (Fig. 1g). Fig. 1h illustrates the dandelion flower-like morphology of the $CuCo_2O_4$/CoS composite. High-resolution SEM imaging in Fig. 1i reveals that these dandelion flower-like structures are composed of nanograss array (NGA)-like structures. This NGA structure potentially offers a high surface area, abundant electroactive sites, and shortened pathways for charge diffusion, facilitating rapid electrolyte transport and consequently enhancing the material's electrochemical performance.

XRD was employed to characterize the crystallinity and phase structure of the $CuCo_2O_4$/CoS composite. The XRD pattern of the $CuCo_2O_4$/CoS composite is presented in Fig. 2. Peaks observed at 2θ values of approximately 19.07°, 31.36°, 36.96°, 38.96°, 45.07°, 56.03°, 59.59°, and 65.75° are attributed to the (111), (220), (311), (222), (400), (422), (511), and (440) planes of the cubic spinel $CuCo_2O_4$ phase (JCPDS #001-1155). Additionally, peaks at 2θ values of approximately 30.8°, 35.5°, 47.2°, 54.8°, 62.9°, 64.1°, and 66.9° correspond to the (100), (101), (102), (110), (103), (200), and (201) planes of hexagonal CoS (JCPDS # 65-3418). These findings align with previously reported literature.[28,29]

To confirm their elemental composition, EDX analysis was conducted on $CuCo_2O_4$, CoS, and $CuCo_2O_4$/CoS samples (Fig. 3). The spectra of the individual $CuCo_2O_4$ and CoS samples showed the existence of only the expected elements: copper (Cu), cobalt (Co), and oxygen (O) for $CuCo_2O_4$; and cobalt (Co) and sulfur (S) for CoS. This indicates the high purity of the synthesized materials. Conversely, the spectrum of the composite material exhibited peaks corresponding to all four elements (Cu, Co, O, and S), confirming the successful integration of $CuCo_2O_4$ and CoS components within the composite structure.

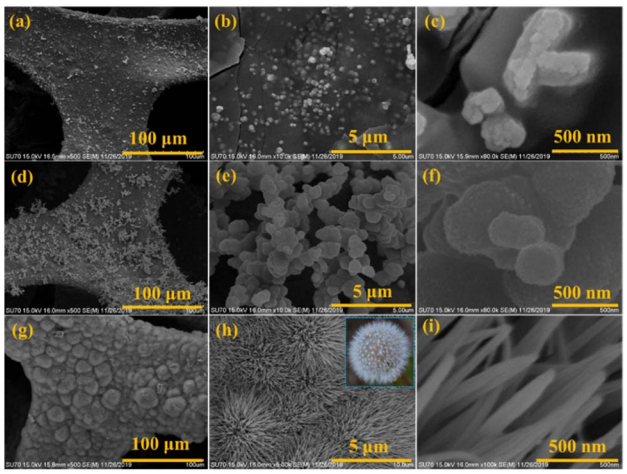

Fig. 1 SEM images at low and high resolution of (a–c) $CuCo_2O_4$, (d–f) CoS, and (g–i) $CuCo_2O_4$/CoS active materials on the Ni foam substrate.

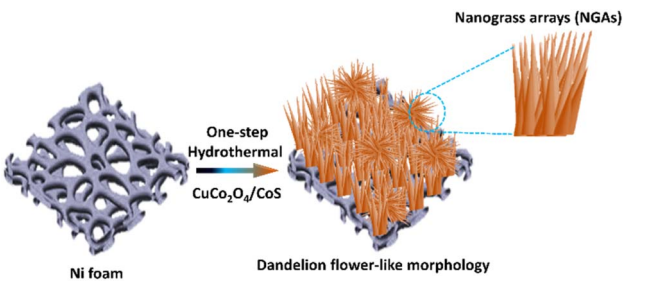

Scheme 1 Schematic representation of the synthesis of dandelion flower-like $CuCo_2O_4$/CoS nanograss arrays on a Ni foam substrate.

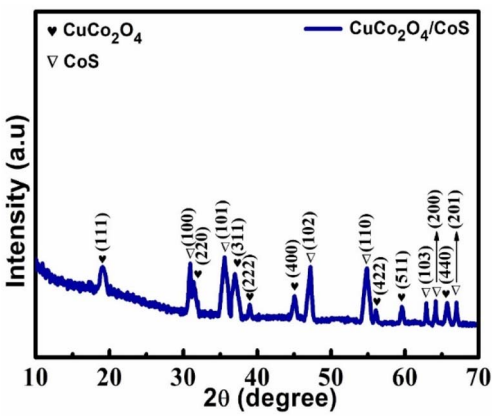

Fig. 2 X-ray diffraction pattern of the as-fabricated $CuCo_2O_4$/CoS composite.

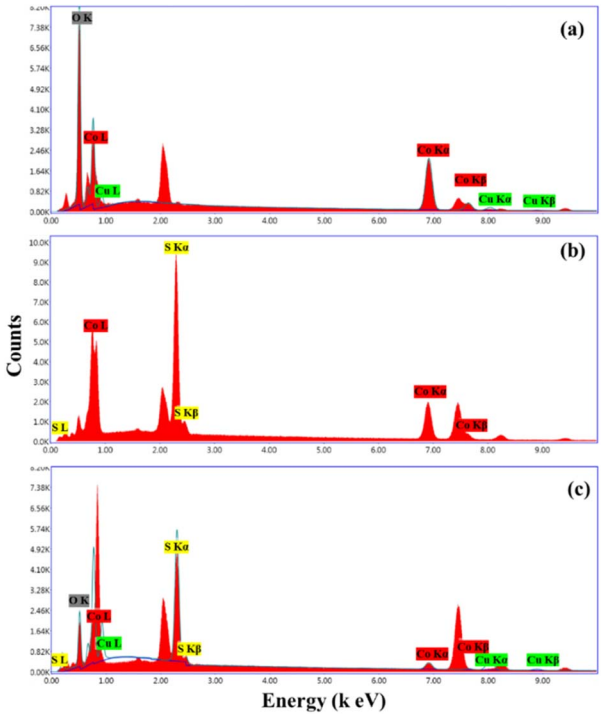

Fig. 3 EDX spectra of (a) $CuCo_2O_4$, (b) CoS, and (c) $CuCo_2O_4$/CoS composite.

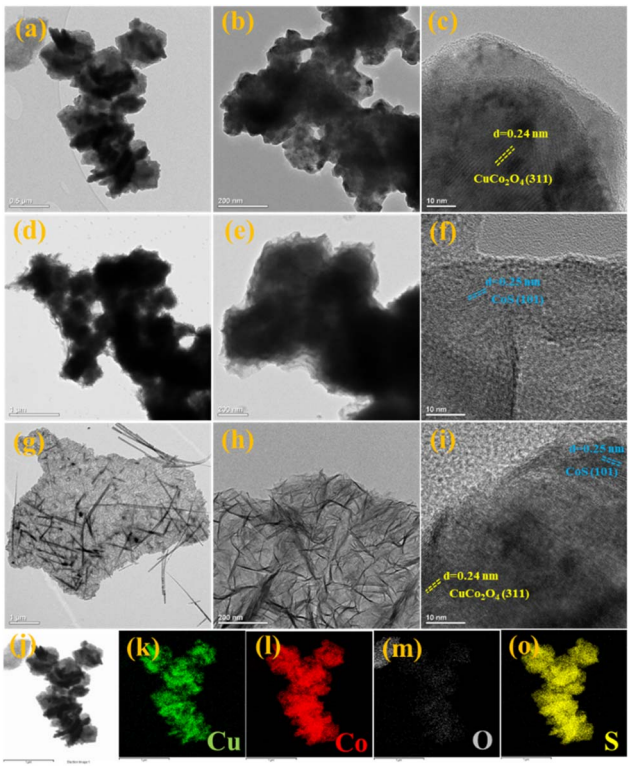

Fig. 4 TEM and high-resolution TEM images of the (a–c) $CuCo_2O_4$, (d–f) CoS, and (g–i) $CuCo_2O_4$/CoS composite electrodes. (j–o) Scanning TEM (STEM) and elemental mapping of the $CuCo_2O_4$/CoS composite electrode.

The $CuCo_2O_4$, CoS, and $CuCo_2O_4$/CoS electrodes were further investigated using TEM, HR-TEM, and scanning TEM (STEM) to examine their morphologies and structural details. As shown in Fig. 4a, b and d, e, TEM images of the $CuCo_2O_4$ and CoS electrodes exhibit agglomerated nanoparticle-like structures, which is consistent with SEM analysis. Furthermore, analysis of HR-TEM images in Fig. 4c and f reveals lattice fringes with 0.24 and 0.25 nm spacings, respectively. These spacings correspond to the (311) and (101) planes of the $CuCo_2O_4$ and CoS phases, respectively.[30,31] In contrast, the $CuCo_2O_4$/CoS composite electrodes display a distinctive hierarchical architecture, with flower-like structures built from interconnected nanograss array-like units (Fig. 4g and h). HR-TEM analysis of the $CuMn_2O_4$/CoS nanostructured electrode (Fig. 4i) reveals interplanar spacings of 0.24 and 0.25 nm, corresponding to the (311) plane of $CuMn_2O_4$ and the (101) plane of CoS, respectively. To further investigate the compositional distribution within the $CuCo_2O_4$/CoS nanostructures, STEM and elemental mapping techniques were utilized. These analyses confirmed the presence and homogeneous distribution of Cu, Co, O, and S within the composite electrode, as evidenced by the elemental maps (Fig. 4j–o).

XPS analysis was employed to delve deeper into the chemical composition and surface chemistry. Fig. S1† displays the survey spectrum of $CuCo_2O_4$/CoS, confirming the presence of Cu, Co, O, and S elements within the sample. High-resolution Cu 2p XPS spectra (Fig. 5a) were deconvoluted, revealing two prominent peaks centered at binding energies of 932.3 eV and 952.1 eV, attributed to Cu $2p_{3/2}$ and Cu $2p_{1/2}$, respectively. Satellite peaks observed at 962.3 eV and 942.2 eV, respectively, accompanying these main peaks, are characteristic of the Cu^{2+} oxidation state.[32] The Co 2p XPS spectrum in Fig. 5b exhibits prominent peaks at 780.5 and 796.2 eV, attributed to Co $2p_{3/2}$ and Co $2p_{1/2}$, respectively, with corresponding satellite peaks at 786.1 and 802.4 eV, indicative of the Co^{2+} oxidation state.[33] The O 1s spectrum in Fig. 5c exhibits a single peak at 531.4 eV,

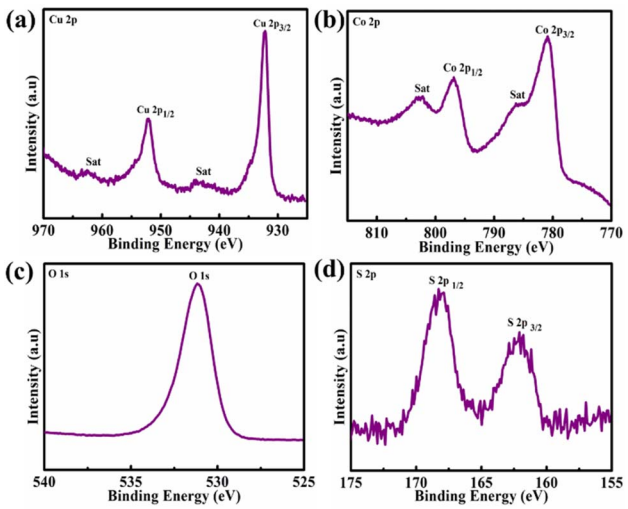

Fig. 5 High-resolution XPS deconvoluted spectra of (a) Cu 2p, (b) Co 2p, (c) O 1s, and (d) S 2p.

indicative of the presence of oxygen ions within the $CuCo_2O_4$ compound.[34] The S 2p spectrum in Fig. 5d exhibits two prominent peaks, corresponding to S $2p_{3/2}$ and S $2p_{1/2}$ at 162.2 and 168.0 eV, respectively, which are characteristic of the S^{2-} state in CoS.[35]

All synthesized materials were characterized using BET and BJH techniques. The adsorption–desorption isotherm of the sample (Fig. 6) exhibited a type IV profile, characteristic of mesoporous materials.[36] The BET analysis revealed that the $CuCo_2O_4$/CoS NGA composite displayed a significantly higher specific surface area (24.3 $m^2\ g^{-1}$) compared to its individual components, $CuCo_2O_4$ (8 $m^2\ g^{-1}$) and CoS (10.6 $m^2\ g^{-1}$). This enhanced surface area provides abundant active sites, potentially facilitating improved electrochemical performance. The inset of Fig. 6 displays the BJH pore size distribution of the samples, indicating average pore sizes of 24.2 nm, 23.1 nm, and 25.6 nm for $CuCo_2O_4$, CoS, and the $CuCo_2O_4$/CoS NGA composite, respectively. These results confirm the mesoporous nature of the materials. The combination of a high specific surface area and mesoporosity, attributed to the substantial pore volume and distinctive nanoflower structures, enhances both electron transport and ion diffusion at the electrolyte–electrode interface. This unique structural characteristic is also pivotal in improving the overall electrochemical performance.

The electrochemical characteristics of $CuCo_2O_4$, CoS, and $CuCo_2O_4$/CoS NGA electrodes were investigated by CV measurements, as demonstrated in Fig. 7. The measurements were done using a standard three-electrode system in 3 M KOH aqueous electrolyte solution over a potential window between −0.3 and 0.5 V *vs.* Ag/AgCl electrode at ambient temperature. Fig. 7a compares CV plots of as-fabricated electrodes at a scan rate of 5 mV s^{-1}. CV curves of the electrodes displayed characteristic redox peaks with significant current, confirming their battery-type behavior. This behavior differs from the capacitive behavior observed in electric double-layer capacitors (EDLCs).[37]

A Faraday reaction may occur within the electrolyte solution as follows.

$$CuCo_2O_4 + H_2O + OH^- \rightarrow CuOOH + 2CoOOH + e^- \quad (2)$$

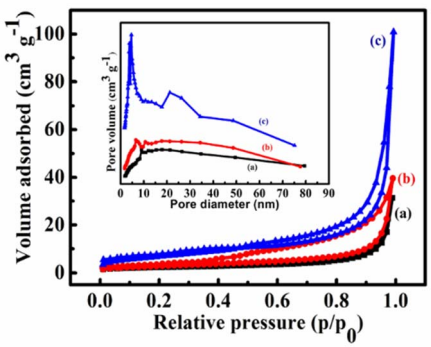

Fig. 6 N_2 adsorption/desorption isotherms with the pore size distribution curve (inset) of the (a) $CuCo_2O_4$, (b) CoS, and (c) $CuCo_2O_4$/CoS electrodes.

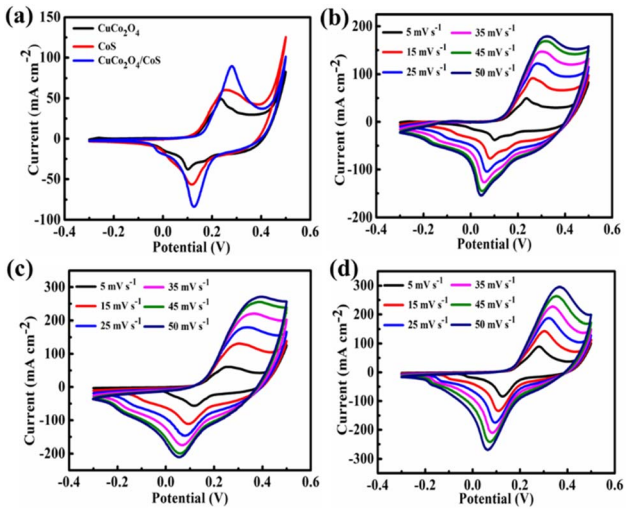

Fig. 7 (a) A comparison of CV plots of $CuCo_2O_4$, CoS, and $CuCo_2O_4$/CoS NGA electrodes at 5 mV s^{-1} scan rate. CV plots of (b) $CuCo_2O_4$, (c) CoS, and (d) $CuCo_2O_4$/CoS NGA electrodes at different scan rates.

$$CoOOH + OH^- \rightarrow CoO_2 + H_2O + e^- \quad (3)$$

$$CoS + OH^- \leftrightarrow CoSOH + e^- \quad (4)$$

$$CoSOH + OH^- \leftrightarrow CoSO + H_2O + e^- \quad (5)$$

Among the tested electrodes at a scan rate of 5 mV s^{-1}, the $CuCo_2O_4$/CoS nanocomposite demonstrated the highest current response in CV measurements, indicated by the largest enclosed area within the CV curve. This enhanced electrochemical activity can be attributed to the significantly increased surface area of the $CuCo_2O_4$/CoS composite. A larger surface area provides more accessible sites for interaction with electrolyte ions, facilitating a higher rate of faradaic reactions. The CV measurements of $CuCo_2O_4$, CoS, and $CuCo_2O_4$/CoS NGA electrodes were carried out at different scan rates from 5 to 50 mV s^{-1}, as shown in Fig. 7b–d, respectively. Cyclic voltammetry (CV) of all three electrodes exhibited characteristic redox peaks indicative of battery-like behavior. Upon increasing the scan rate, a positive shift in the anodic peak and a negative shift in the cathodic peak were observed in the CV curves of the prepared electrodes. This phenomenon is attributed to the increasing internal diffusion limitations within the three-electrode system.[38] Despite this shift, the peak shape remains unchanged, indicating a good rate capability.

A common method to explore charge storage mechanisms in fabricated electrode materials involves analyzing the relationship between cathodic peak current (i_p) and scan rate (v) using a power law ($i_p = av^b$).[39] The slope 'b' of the $\log(v) - \log(i_p)$ plot provides valuable insights. Typically, a 'b' value close to 0.5 indicates diffusion-controlled charge storage, characteristic of battery-type behavior. Conversely, a 'b' value near 1.0 suggests surface-controlled processes, typical of capacitive behavior. The b values obtained for the present study were found to be (Fig. 7a) 0.548, 0.641, and 0.51 for $CuCo_2O_4$, CoS, and $CuCo_2O_4$/CoS NGA electrodes, respectively. The results strongly suggest that the

fabricated electrode materials exhibit primarily diffusion-controlled behavior, a characteristic often observed in battery-type electroactive materials.[40]

The precise quantification of capacitive and diffusion-controlled charge storage contributions in the synthesized electrodes can be achieved using the following equation.[41]

$$i_p = k_1 v + k_2 v^{1/2} \quad (6)$$

where k_1 (slope) and k_2 (intercept) are constants determined from the linear relationship between $i/v^{1/2}$ *vs.* $v^{1/2}$. A linear regression analysis of $CuCo_2O_4$, CoS, and $CuCo_2O_4$@CoS datasets revealed k_1 values of 0.0002322, 0.00020082, and 0.0000442, respectively, and corresponding k_2 values of 0.01255, 0.01599, and 0.01179, respectively. Fig. 6a and b present the calculated relative contributions of faradaic and diffusion-controlled processes derived from the obtained values of k_1 and k_2. The relative contributions of diffusion-controlled and surface-controlled processes in redox reactions at an electrode shift with scan rate, with slower scans favoring diffusion-limited reactions due to increased ion penetration, and faster scans emphasizing capacitive contributions from the electrode–electrolyte interface. Fig. 8b–d support these observations, demonstrating that the contribution from diffusion diminishes progressively as the scan rate increases for the pristine electrodes. Significantly, the composite $CuCo_2O_4$@CoS electrode consistently demonstrates a greater contribution from diffusion-controlled charge storage than $CuCo_2O_4$ and CoS electrodes across all scan rates. This enhanced diffusional contribution aligns with the observed superior rate performance of $CuCo_2O_4$@CoS. This suggests that the composite material facilitates a slower redox reaction kinetics during electrochemical processes.

The electrochemical performance of electrode materials was further measured using GCD measurements. Fig. 9a shows the comparative GCD curves of $CuCo_2O_4$, CoS, and composite $CuCo_2O_4$/CoS NGA electrodes at the same current density of 6 mA cm^{-2}. All the GCD curves exhibit the typical faradaic redox battery-type nature of electrode materials, which is consistent with the obtained CV results. As expected, the $CuCo_2O_4$/CoS NGA composite electrode shows a much longer discharge time than the $CuCo_2O_4$ and CoS electrodes at a current density of 6 mA cm^{-2}. Fig. 9b–d show the GCD curves of $CuCo_2O_4$, CoS, and composite $CuCo_2O_4$/CoS NGA electrodes at different current densities varying from 6 to 50 mA cm^{-2}.

The specific capacity values of the three electrodes were calculated using GCD plots and eqn (1), and the corresponding results are plotted in Fig. 9e. As shown in Fig. 9e, the $CuCo_2O_4$/CoS NGA composite electrode exhibits excellent specific capacity values of 217.86, 209.78, 192.77, 180.6, 169.64, and 140.08 mA h g^{-1} at current densities of 6, 8, 15, 20, 30, and 50 mA cm^{-2}, respectively, much higher than those of the $CuCo_2O_4$ (142.54, 136.21, 115.07, 90.19, 87.24, and 81.58 mA h g^{-1}) and CoS (160.37, 156.71, 147.07, 139.71, 127.47, and 110.6 mA h g^{-1}) electrodes, respectively. The observed enhanced electrochemical performance of the $CuCo_2O_4$/CoS NGA composite electrode can be attributed to several factors, including an increased surface area, improved conductivity, and facilitated ion transport. These benefits likely stem from the unique

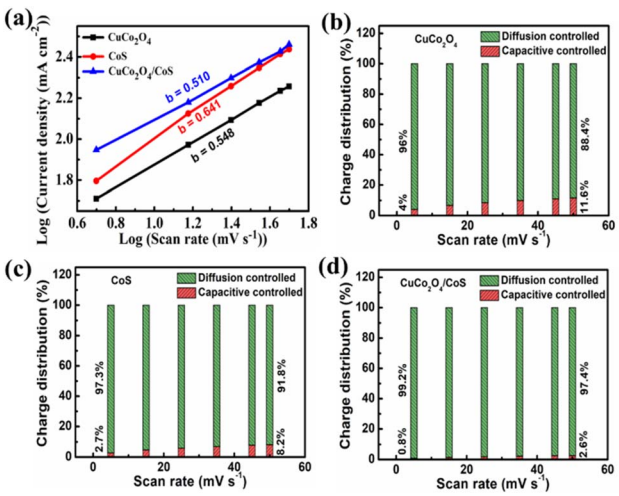

Fig. 8 (a) The *b*-value for the cathodic peaks of the as-prepared samples was determined from the slope of the log(*i*) *vs.* log(scan rate, *v*) plot. Investigation of charge storage contributions in (b) $CuCo_2O_4$, (c) CoS, and (d) $CuCo_2O_4$/CoS NGA electrodes by analysing their dependence on the scan rate.

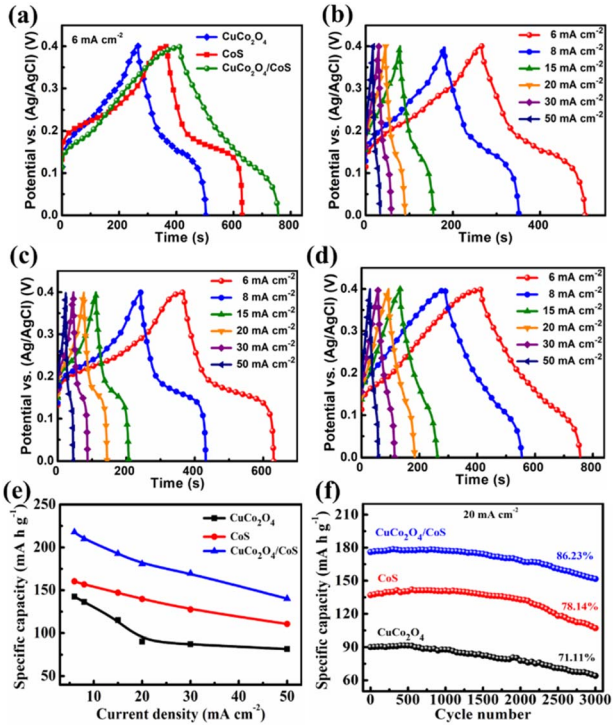

Fig. 9 (a) Comparative GCD plots of the $CuCo_2O_4$, CoS, and $CuCo_2O_4$/CoS NGA electrodes at a current density of 6 mA cm^{-2}. GCD curves of the (b) $CuCo_2O_4$, (c) CoS, and (d) $CuCo_2O_4$/CoS electrodes at various current densities. (e) Specific capacity of $CuCo_2O_4$, CoS, and composite $CuCo_2O_4$/CoS NGA electrodes at different current densities. (f) The cycling performance of $CuCo_2O_4$, CoS, and composite $CuCo_2O_4$/CoS NGA electrodes at 20 mA cm^{-2} over 3000 cycles.

Table 1 Comparison of the specific capacity of the $CuCo_2O_4$/CoS NGA composite electrode with recent reports

Electrode materials	Preparation method	Electrolyte	Specific capacity, mA h g^{-1}	Current density	Reference
$CuCo_2O_4$	Solvothermal	2 M KOH	109.35	1 A g^{-1}	42
$CuCo_2O_4$/rGO	Self-assembly	6 M KOH	40.4	1 A g^{-1}	43
$CuCo_2O_4$@$Co(OH)_2$	Hydrothermal and electrodeposition	1 M KOH	23.78	0.5 A g^{-1}	44
$CuCo_2O_4$/CuO	Microwave assisted reflux	1 M KOH	49.86	1 A g^{-1}	45
$CuCo_2O_4$@C	Hydrothermal and magnetron sputtering	2 M NaOH	198.94	1 A g^{-1}	46
$CuCo_2O_4$/CuO	Hydrothermal deposition and SILAR	1 M KOH	79.22	11 mA cm^{-2}	47
$CuCo_2O_4$@$NiCo_2O_4$	Two-step hydrothermal	2 M KOH	105.5	1 A g^{-1}	48
$NiCo_2O_4$@CuS	Two-step hydrothermal	3 M KOH	141.13	1 A g^{-1}	49
$CuCo_2O_4$/CuS	Hydrothermal and thermolysis	3 M KOH	102.1	1 A g^{-1}	50
$CuCo_2O_4$/$MnCo_2O_4$	Two-step hydrothermal	2 M KOH	199.16	0.5 A g^{-1}	24
$CuCo_2O_4$/CoS	**One-step hydrothermal**	**3 M KOH**	**217.86**	**6 mA cm^{-2}**	**This study**

hierarchical and interpenetrating network structure of the $CuCo_2O_4$/CoS composite, making it a promising candidate for supercapacitor applications. The $CuCo_2O_4$/CoS NGA composite electrode exhibited a superior specific capacity value compared to both individual $CuCo_2O_4$ and CoS nanocomposite electrodes, as well as surpassing values reported in previous literature, as listed in Table 1.

Long-term cycling stability is essential for the practical viability of nanocomposite electrode materials. As shown in Fig. 9f, the cycling stability of $CuCo_2O_4$, CoS, and composite $CuCo_2O_4$/CoS NGA electrodes was determined at a current density of 20 mA cm^{-2} over 3000 cycles. A significant improvement in cycling stability was observed in the $CuCo_2O_4$/CoS NGA composite electrode compared to its individual components, $CuCo_2O_4$ and CoS. After 3000 cycles, the composite electrode retained 86.23% of its initial capacitance, while $CuCo_2O_4$ and CoS retained 71.11% and 78.14%, respectively. This enhanced stability can be attributed to the synergistic effects between $CuCo_2O_4$ and CoS within the composite structure. Combining these materials may improve charge transfer kinetics, reduce volume changes during cycling, and enhance structural stability, leading to improved long-term performance.

EIS is an effective diagnostic technique to explore further the excellent electrochemical behaviours of the as-prepared electrode materials. The Nyquist plots of $CuCo_2O_4$, CoS, and composite $CuCo_2O_4$/CoS NGA electrodes in 3 M KOH electrolyte are presented in Fig. 10, and the equivalent circuit is shown in the inset of the figure to fit the Nyquist plots. Nyquist plots typically exhibit two distinct regions: a semicircle in the high-frequency range and a sloped line in the low-frequency range. The *x*-intercept of the semicircle in the high-frequency region corresponds to the equivalent series resistance (R_s), while the diameter of the semicircle is often associated with the charge transfer resistance (R_{ct}) at the electrode–electrolyte interface.[51] The R_s (0.3 Ω cm^{-2}) and R_{ct} (0.57 Ω cm^{-2}) values of the composite $CuCo_2O_4$/CoS NGA electrode are lower than those of the bare $CuCo_2O_4$ ($R_s = 0.46$ Ω cm^{-2} and $R_{ct} = 1.11$ Ω cm^{-2}) and CoS ($R_s = 0.35$ Ω cm^{-2} and $R_{ct} = 0.88$ Ω cm^{-2}) electrodes. The composite $CuCo_2O_4$/CoS NGA electrode has the lowest R_s and R_{ct} values and steeper linear slope than the bare $CuCo_2O_4$ and CoS electrodes, which further demonstrate the superior ion diffusion, improved charge transfer kinetics, enhanced electrical conductivity, and improved ionic conductivity.[52]

The $CuCo_2O_4$/CoS nanograss electrode material, grown directly on a Ni foam substrate, exhibits enhanced energy storage performance. Fig. 10b illustrates a schematic diagram of the $CuCo_2O_4$/CoS nanograss electrode, highlighting key features for efficient electron transport and OH^- ion penetration. The 3D Ni foam scaffold provides a conductive backbone, facilitating rapid ion and electron transport. The direct growth of nanograss arrays eliminates the need for binders and additives, minimizing dead mass and improving electron conductivity. The high surface area of the nanograss arrays maximizes active site exposure, enabling fast electrochemical reactions. Furthermore, the robust adhesion of the nanograss arrays to the substrate ensures long-term cycling stability. The vertically aligned structure of the nanograss arrays shortens the diffusion pathways for electrolyte ions, contributing to high areal capacity and stable cycling performance. These combined factors result in superior ionic and electronic conductivity within the composite, making it a promising battery-type electrode material for high-performance hybrid supercapacitors.

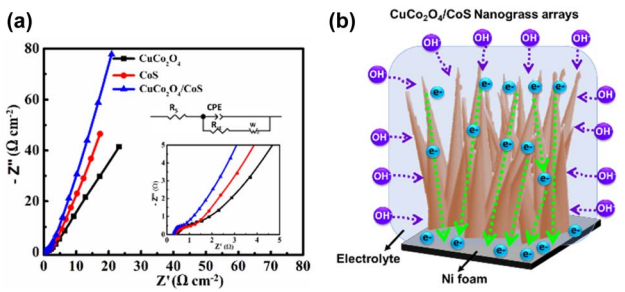

Fig. 10 (a) EIS Nyquist plots of $CuCo_2O_4$, CoS, and composite $CuCo_2O_4$/CoS NGA electrodes. The inset displays high-magnification Nyquist plots alongside the corresponding equivalent circuit to fit the plots. (b) Schematic diagram illustrating the merits of the $CuCo_2O_4$/CoS nanograss array electrode.

4 Conclusion

In summary, hierarchical dandelion flower-like $CuCo_2O_4$/CoS structures were successfully developed on Ni foam *via* a facile

and effective one-step hydrothermal process. The surface morphology results reveal that the dandelion flower-like structures consist of nanograss arrays. The hierarchical architecture offers several key benefits, including increased surface area, enhanced electrolyte ion diffusion, shortened ion transport pathways, and excellent conductivity, all contributing to superior overall electrochemical performance. CV and GCD measurements demonstrated that the fabricated $CuCo_2O_4$, CoS, and composite $CuCo_2O_4$/CoS NGA electrodes exhibited electrochemical characteristics typical of a faradaic redox battery-type behavior. The as-prepared composite $CuCo_2O_4$/CoS NGA electrode exhibited superior electrochemical performance with an ultrahigh specific capacity of 217.86 mA h g^{-1} at 6 mA cm^{-2} compared to $CuCo_2O_4$ (142.54 mA h g^{-1}) and CoS (160.37 mA h g^{-1}) electrodes. Furthermore, the composite $CuCo_2O_4$/CoS NGA electrode demonstrated enhanced cycling stability, retaining 87.37% of its initial capacity after 3000 cycles, surpassing the performance of individual $CuCo_2O_4$ (71.11%) and CoS (78.14%) electrodes. Furthermore, EIS analysis revealed that the composite $CuCo_2O_4$/CoS NGA electrode exhibited lower charge transfer resistance and solution resistance than individual $CuCo_2O_4$ and CoS electrodes, indicating enhanced charge transfer kinetics, improved conductivity, and superior ion diffusion. Therefore, our findings demonstrate that the synthesized battery-type $CuCo_2O_4$/CoS NGA composite electrode exhibits exceptional potential as an electrode material for supercapacitor applications.

Data availability

The data supporting this study's findings are available from the corresponding author upon reasonable request.

Author contributions

Chandu V. V. Muralee Gopi: writing – original draft, conceptualization, methodology, formal analysis, investigation, writing – review & editing; Araveeti Eswar Reddy: writing – original draft, conceptualization, methodology, formal analysis, investigation, writing – review & editing; S. S. Rao: investigation, methodology; K. V. G. Raghavendra: investigation, methodology; M. Suneetha: funding, formal analysis, investigation, supervision, validation; H. J. Kim: funding, formal analysis, investigation, supervision, validation.

Conflicts of interest

There are no conflicts to declare.

Acknowledgements

This study was supported by the Basic Science Research Program through the National Research Foundation of Korea (NRF) funded by the Korea Ministry of Education (2016R1D1A1B02009234) and the Ministry of Trade, Industry, and Energy (Grant No. 0002310). This work was supported by the National Research Foundation of Korea (NRF) (Grant No. RS-2022-00166999). This work was also supported by the Adama Science and Technology University.

References

1 S. Nayak, A. A. Kittur, S. Nayak and B. Murgunde, *J. Energy Storage*, 2023, **62**, 106963.
2 J. Wang, P. Nie, B. Ding, S. Dong, X. Hao, H. Dou and X. Zhang, *J. Mater. Chem. A*, 2017, **5**, 2411–2428.
3 Y. Zhang, T. Cheng, Y. Wang, W. Lai, H. Pang and W. Huang, *Adv. Mater.*, 2016, **28**, 5242–5248.
4 J. Xiao, L. Wan, S. Yang, F. Xiao and S. Wang, *Nano Lett.*, 2014, **14**, 831–838.
5 L. Kunhikrishnan and R. Shanmugham, *Mater. Charact.*, 2021, **177**, 111160.
6 Z. Deng, H. Jiang, Y. Hu, Y. Liu, L. Zhang, H. Liu and C. Li, *Adv. Mater.*, 2017, **29**, 1603020.
7 Y. Yang, Y. Ma, C. Lu, S. Li and M. Zhu, *Green Chem.*, 2023, **25**, 10209–10234.
8 M. Salanne, B. Rotenberg, K. Naoi, K. Kaneko, P.-L. Taberna, C. P. Grey, B. Dunn and P. Simon, *Nat. Energy*, 2016, **1**, 16070.
9 H. H. Li, J. Song, L. I. Wang, X. M. Feng, R. Q. Liu, W. J. Zeng, Z. D. Huang, Y. W. Ma and L. H. Wang, *Nanoscale*, 2017, **9**, 193–200.
10 Z. Wang, Y. Long, D. Cao, D. Han and F. Gu, *Electrochim. Acta*, 2019, **307**, 341–350.
11 M. Li, J. Yu, X. Wang and Z. Yang, *Appl. Surf. Sci.*, 2020, **530**, 147230.
12 J. Zhu, S. Tang, J. Wu, X. Shi, B. Zhu and X. Meng, *Adv. Energy Mater.*, 2017, **7**, 1601234–1601245.
13 X. Zhao, B. M. Sanchez, P. J. Dobson and P. S. Grant, *Nanoscale*, 2011, **3**, 839–855.
14 X. Ge, Y. Liu, F. W. T. Goh, T. S. A. Hor, Y. Zong, P. Xiao, Z. Zhang, S. H. Lim, B. Li, X. Wang and Z. Liu, *ACS Appl. Mater. Interfaces*, 2014, **6**, 12684–12691.
15 S. G. Krishnan, M. V. Reddy, M. Harilal, B. Vidyadharan, I. I. Misnon, M. H. A. Rahim, J. Ismail and R. Jose, *Electrochim. Acta*, 2015, **161**, 312–321.
16 L. Lin, S. Tang, S. Zhao, X. Peng and N. Hu, *Electrochim. Acta*, 2017, **228**, 175–182.
17 S. Vijayakumar, S. H. Lee and K. S. Ryu, *Electrochim. Acta*, 2015, **182**, 979–986.
18 G. Gao, H. B. Wu, S. Ding, L. M. Liu and X. W. Lou, *Small*, 2015, **11**, 804–808.
19 B. Guan, D. Guo, L. Hu, G. Zhang, T. Fu, W. Ren, J. Li and Q. Li, *J. Mater. Chem. A*, 2014, **2**, 16116–16123.
20 L. Liao, H. Zhang, W. Li, X. Huang, Z. Xiao, K. Xu, J. Yang, R. Zou and J. Hu, *J. Alloys Compd.*, 2017, **695**, 3503–3510.
21 Y. Zhang, J. Xu, Y. Zheng, Y. Zhang, X. Hu and T. Xu, *RSC Adv.*, 2017, **7**, 3983–3991.
22 K. Qiu, M. Lu, Y. Luo and X. Du, *J. Mater. Chem. A*, 2017, **5**, 5820–5828.
23 A. Pendashteh, M. S. Rahmanifar, R. B. Kaner and M. F. Mousavi, *Chem. Commun.*, 2014, **50**, 1972–1975.
24 S. Liu, K. S. Hui, K. N. Hui, J. M. Yun and K. H. Kim, *J. Mater. Chem. A*, 2016, **4**, 8061–8071.

25 K. Xu, S. Li, J. Yang, H. Xu and J. Hu, *J. Alloys Compd.*, 2016, **678**, 120–125.
26 J. Nallapureddy, M. R. Pallavolu, P. S. Srinivasa Babu, B. A. Al-Asbahi and S. W. Joo, *Energy Fuel*, 2023, **37**, 17535–17544.
27 A. E. Reddy, T. Anitha, C. V. V. M. Gopi, S. S. Rao and H. J. Kim, *Dalton Trans.*, 2018, **47**, 9057–9063.
28 F. S. Omar, A. Numan, N. Duraisamy, M. M. Ramly, K. Ramesh and S. Ramesh, *Electrochim. Acta*, 2017, **227**, 41–48.
29 K. A. Kumar, A. Pandurangan, S. Arumugam and M. Sathiskumar, *Sci. Rep.*, 2019, **9**, 1228.
30 R. Yang, J. Yesuraj, J. Kim and K. Kim, *Electrochim. Acta*, 2023, **437**, 141507.
31 D. Ma, B. Hu, W. Wu, X. Liu, *et al.*, *Nat. Commun.*, 2019, **10**, 3367.
32 X. Luo, M. Huang, L. Bie, D. He, Y. Zhang and P. Jiang, *RSC Adv.*, 2017, **7**, 23093–23101.
33 J. Tang, Y. Ge, J. Shen and M. Ye, *Chem. Commun.*, 2016, **52**, 1509–1512.
34 H. J. Kim, D. J. Kim, T. Anitha, Y. A. Kumar, J. S. Bak, I. Cho, M. Jagadeesh and A. E. Reddy, *New J. Chem.*, 2019, **43**, 15605–15613.
35 S. Li, J. Wen, T. Chen, L. Xiong, J. Wang and G. Fang, *Nanotechnology*, 2016, **27**, 145401.
36 T. Anitha, A. E. Reddy, Y. A. Kumar, Y. R. Cho and H. J. Kim, *Dalton Trans.*, 2019, **48**, 10652–10660.
37 Z. Song, Y. Zhang, W. Liu, S. Zhang, G. Liu, H. Chen and J. Qiu, *Electrochim. Acta*, 2013, **112**, 120–126.
38 C. Young, R. R. Salunkhe, S. M. Alshehri, T. Ahamad, Z. Huang, J. Henzie and Y. Yamauchi, *J. Mater. Chem. A*, 2017, **5**, 11834–11839.
39 B. Y. Guan, L. Yu, X. Wang, S. Song and X. W. D. Lou, *Adv. Mater.*, 2016, **29**, 1605051.
40 H. D. Chul, R. Vinodh, C. V. V. M. Gopi, C. Deviprasath, H. J. Kim and M. S. Ki, *Dalton Trans.*, 2019, **48**, 14808–14819.
41 C. Ren, *et al.*, *Adv. Funct. Mater.*, 2020, **30**, 2004519.
42 J. Sun, X. Tian, C. Xu and H. Chen, *J. Mater.*, 2021, **7**, 1358–1368.
43 P. Liang, F. Wang and Z. A. Hu, *Chem. Eng. J.*, 2018, **350**, 627–636.
44 Y. Zhang, H. Liu, M. Huang, J. M. Zhang, W. Zhang, F. Dong and Y. X. Zhang, *ChemElectroChem*, 2017, **4**, 721–727.
45 A. Shanmugavani and R. K. selvan, *Electrochim. Acta*, 2016, **188**, 852–862.
46 H. Yan, Y. Lu, K. Zhu, T. Peng, X. Liu, Y. Liu and Y. Luo, *Appl. Surf. Sci.*, 2018, **439**, 883–890.
47 G. P. Kamble, *et al.*, *ACS Appl. Nano Mater.*, 2021, **4**, 12702–12711.
48 B. Nawaz, M. O. Ullah and G. Ali, *Energies*, 2021, **14**, 3237.
49 C. V. V. M. Gopi, D. K. Kulurumotlakatla, K. V. G. Raghavendra, M. Suneetha and R. Ramesh, *RSC Adv.*, 2024, **14**, 40087–40097.
50 Z. K. Heiba, M. A. Deyab, M. B. Mohamed, N. M. Farag, A. M. El-naggar and J. R. Plaisier, *Appl. Phys. A*, 2021, **127**, 853.
51 A. E. Reddy, T. Anitha, C. V. V. M. Gopi, I. K. Durga and H. J. Kim, *New J. Chem.*, 2018, **42**, 2964–2969.
52 F. Li, Y. X. Zhang, M. Huang, Y. Xing and L. L. Zhang, *Electrochim. Acta*, 2015, **154**, 329–337.